Silica Nanoparticle Architecture Determines Radiative Properties of Encapsulated Fluorophores

Daniel R. Larson,[†,‡] Hooisweng Ow,[§,||] Harshad D. Vishwasrao,[†] Ahmed A. Heikal,[⊥] Ulrich Wiesner,*[,§] and Watt W. Webb*[,†]

School of Applied and Engineering Physics and Department of Materials Science and Engineering, Cornell University, Ithaca, New York 14853, and Department of Bioengineering, Pennsylvania State University, University Park, Pennsylvania 16802

Received September 19, 2007. Revised Manuscript Received January 3, 2008

Silica nanoparticles with embedded fluorescent molecules are used in a variety of applications requiring the observation of single nanoprobes. We describe a class of fluorescent, core–shell silica nanoparticles with a radius of ~15 nm, narrow particle size distribution, and controlled internal architecture. Particles covalently encapsulating multiple rhodamine molecules are over 20 times brighter than the single dye molecule in water. The photophysical behavior of rhodamine can be manipulated by small changes in the internal architecture of particles with otherwise similar composition, leading to 3-fold enhancement of quantum efficiency per dye with no observable energy transfer between neighboring dyes. This enhancement of quantum efficiency per dye is due to a uniform 2-fold enhancement in radiative rate and a variable reduction in nonradiative rate which varies inversely with the degree of rotational mobility of the dye allowed by the particle architecture. These results demonstrate a practical method for synthesizing highly fluorescent silica nanoparticles and an effective methodology for selectively modifying the photophysical properties of fluorophores.

Introduction

Two general approaches have emerged in recent years for synthesizing highly fluorescent, water-soluble nanoparticles for use in a range of demanding biological and analytical applications. In the first approach, the nanoparticulate material itself is fluorescent (such as semiconductor nanocrystals or metal nanocrystals).[1–6] In the second approach, the fluorescent nanoparticles are based on the incorporation of organic dye molecules into nanoparticles.[7–10] Given the vast diversity of organic dye molecules and the exquisite sensitivity of these dye molecules to their local environment, the latter approach raises the possibility of developing nanoparticles with a broad range of precisely controlled fluorescence characteristics. Here, we describe a class of silica nanoparticles with radii of ~15 nm in which the internal architecture of the silica particle has marked effects on the radiative properties of the constituent dye.

On the basis of the pioneering work of Stöber and coworkers,[11] silica nanoparticles with embedded dye have been synthesized in a range of sizes, colors, and architectures.[9,12–21] In previous reports of photophysical properties, the dye which is covalently bound inside the silica particle is observed to be quenched in comparison to the free dye.[9,13,16–18] However, in the case of poly(organosiloxane) microgels in which the dye is noncovalently attached and loaded through diffusion,

* Corresponding authors. Tel., +1 607 255-3331; fax, +1 607 255-7658; e-mail, www2@cornell.edu (W.W.W.). Tel., +1 607 255-3487; fax, +1 607 255-2365; e-mail, uli@ccmr.cornell.edu (U.W.).

† School of Applied and Engineering Physics, Cornell University.

‡ Present address: Department of Anatomy and Structural Biology, Albert Einstein College of Medicine, Bronx, New York 10461.

§ Department of Materials Science and Engineering, Cornell University.

|| Present address: Hybrid Silica Technologies, Inc., Suite 127 Langmuir Laboratories, 95 Brown Road #1033, Ithaca, New York 14850.

⊥ Pennsylvania State University.

(1) Chan, W.; Maxwell, D. J.; Xiaohu, G.; Bailey, R. E.; Han, M.; Nie, S. *Curr. Opin. Biotechnol.* **2002**, *13*, 40.
(2) Gerion, D.; Pinaud, F.; Williams, S. C.; Parak, W. J.; Zanchet, D.; Weiss, S. Alivisatos, P. *J. Phys. Chem. B* **2001**, *105*, 8861.
(3) Mattoussi, H.; Mauro, J. M.; Goldman, E. R.; Anderson, G. P.; Sundar, V. C.; Mikulec, F. V.; Bawendi, M. G. *J. Am. Chem. Soc.* **2000**, *122*, 12142.
(4) Dubertret, B.; Skourides, P.; Norris, D. J.; Noireaux, V.; Brivanlou, A. H.; Libchaber, A. *Science* **2002**, *298*, 1759.
(5) Larson, D. R.; Zipfel, W. R.; Williams, R. M.; Clark, S. W.; Bruchez, M. P.; Wise, F. W.; Webb, W. W. *Science.* **2003**, *300* (5624), 1434.
(6) Zheng, J.; Petty, J. T.; Dickson, R. M. *J. Am. Chem. Soc.* **2003**, *125*, 7780.
(7) Erhardt, R.; Zhang, M.; Böker, A.; Zettl, H.; Abetz, C.; Frederik, P.; Krausch, G.; Abetz, V.; Müller, A. H. E. *J. Am. Chem. Soc.* **2003**, *125*, 3260.
(8) Minard-Basquin, C.; Weil, T.; Hohner, A.; Rädler, J. O.; Müllen, K. *J. Am. Chem. Soc.* **2003**, *125*, 5832.
(9) Nyffenegger, R.; Quellet, C.; Ricka, J. *J. Colloid Interface Sci.* **1993**, *159*, 150.
(10) Dullens, R. P. A.; Claesson, M.; Derks, D.; van Blaaderen, A.; Kegel, W. K. *Langmuir* **2003**, *19* (15), 5963.
(11) Stöber, W.; Fink, A.; Bohn, E. *J. Colloid Interface Sci.* **1968**, *26*, 62.
(12) van Blaaderen, A.; Peetermans, J.; Maret, G.; Dhont, J. K. G. *J. Chem. Phys.* **1992**, *96*, 4591.
(13) van Blaaderen, A.; Vrij, A. *Langmuir* **1992**, *8*, 2921.
(14) Lettinga, M. P.; van Zandvoort, M. A. M. J.; van Kats, C. M.; Philipse, A. P. *Langmuir* **2000**, *16*, 6156.
(15) Verhaegh, N. A. M.; van Blaaderen, A. *Langmuir* **1994**, *10*, 1427.
(16) Imhof, A.; Megens, M.; Engelberts, J. J.; de Lang, D. T. N.; Sprik, R.; Vos, W. L. *J. Phys. Chem. B* **1999**, *103*, 1408.
(17) Makarova, O. V.; Ostafin, A. E.; Miyoshi, H.; Norris, J. R. *J. Phys. Chem. B* **1999**, *103*, 9080.
(18) Dewar, P. J.; MacGillivray, T. F.; Crispo, S. M.; Smith-Palmer, T. *J. Colloid Interface Sci.* **2000**, *228*, 253.
(19) Bele, M.; Siiman, O.; Matijevic, E *J. Colloid Interface Sci.* **2002**, *254*, 274.
(20) Wang, F. T., W. B.; Zhang, Y.; Fan, X.; Wang, M. *Nanotechnology* **2006**, *17*, R1.
(21) Burns, A.; Ow, H.; Wiesner, U. *Chem. Soc. Rev.* **2006**, *35*, 1028.

10.1021/cm7026866 CCC: $40.75
Published on Web 03/15/2008

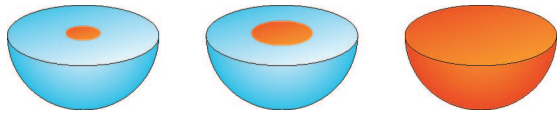

Figure 1. Schematic of three different silica nanoparticle architectures, designated from left to right as the compact core–shell particle, the expanded core–shell particle, and the homogeneous particle. Blue designates silica without dye molecules; orange designates a composite silica dye matrix.

a slight increase in fluorescence efficiency is observed.[22] The quantum efficiency of the embedded dye in polystyrene microspheres is the same or less than that of the free dye.[23] The fluorescence quenching mechanism in these systems is either intraparticle energy transfer or some other nonradiative pathway (e.g., molecule−molecule interaction, electron transfer, isomerization) within the solid matrix. These pathways are likely to be influenced by the local dye environment within the particle, suggesting that precise control of the architecture within the particle might ameliorate quenching or even lead to fluorescence enhancement.

We recently described the development of core–shell fluorescent silica nanoparticles with narrow size distributions and a radius of 15 nm.[24] In these particles, referred to as C dots, the core is composed of multiple organic dyes (e.g., tetramethylrhodamine) covalently bonded to an organically modified silica framework surrounded by a siliceous shell, and the fluorescent properties of the particle were found to depend on the presence or absence of the protective silica shell. In the present work, we have developed architectural variations on this basic core–shell morphology to achieve desired enhancements of the fluorescence properties, for example, increased quantum efficiency and particle brightness (Figure 1). These three architectures are (1) a compact core containing dye surrounded by a silica shell, (2) a slightly expanded core containing dye surrounded by the shell, and (3) a homogeneous particle with dye molecules sparsely embedded within. All three particles have approximately the same size and composition, but the constituent dyes exhibit different photophysical properties. We achieve greater than 3-fold increase in the quantum efficiency of fluorescence of tetramethylrhodamine by optimizing the nanoparticle structure. Each architecture gives a 2-fold enhanced radiative rate for the constituent dye. The reduction in nonradiative rate varies by a factor of 3 between the architectures, with the nonradiative rate of the homogeneous particle being the lowest. These changes in nonradiative rates correlate with the restricted rotational mobility of the dye covalently bound within the particle: the more restricted the mobility, the smaller the nonradiative rate. In addition, we have seen no direct evidence for intraparticle energy transfer between dye molecules. The ability to control photophysical properties through nanoparticle architecture enables both the development of the next generation of fluorescent probes and the study of fluorescent properties that might be inaccessible in solution.

(22) Graf, C.; Schärtl, W.; Fischer, K.; Hugenberg, N.; Schmidt, M. *Langmuir* **1999**, *15*, 6170.
(23) Wittmerhaus, B.; Skibicki, J. J.; McLafferty, J. B.; Zhang, Y.-Z.; Swan, S. *J. Fluoresc.* **2001**, *11* (2), 119.
(24) Ow, H.; Larson, D. R.; Srivastava, M.; Baird, B. A.; Webb, W. W.; Wiesner, U. *Nano Lett.* **2005**, *5* (1), 113.

Materials and Methods

Synthesis. The amounts of adducts for synthesis of the three different silica particle constructs are identical. All reactions were conducted in 1 L batches. It is the order in which the reagents are reacted that leads to different particle architectures. Specifically, all three reaction batches in ethyl alcohol (Aldrich) solvent contain 0.2 M ammonia (Aldrich), 0.155 M tetraethylorthosilicate (TEOS; Aldrich), and 0.855 M deionized water (18.2 MΩ, Barnstead Nanopure DIamond). Because the amounts of reagents are identical in all three different synthesis protocols, the resultant silica nanoparticles are similar in size. However, the chemical environment around the dye molecules in each construct is expected to be quite different with respect to silica matrix density and presence of organic moieties. All chemicals were used as received without further purification. Dye precursor was synthesized by addition reaction between tetramethylrhodamine isothiocyanate (TRITC; Molecular Probes) and 3-aminopropyltriethoxysilane (Aldrich) in molar ratio of 1:50, in exclusion of moisture.[13] The core–shell nanoparticle synthesis protocols were modified from the classic Stöber protocol, similar to what was previously described by Nyffenegger and co-workers as heterogeneous nucleation, whereas particles with homogeneous dye distribution were synthesized via homogeneous nucleation.[9] For the synthesis of nanoparticles with compact core architecture, the aforementioned dye precursor, usually containing around 1.70×10^{-5} M of TRITC, was added to the reaction vessel containing appropriate amounts of ammonia, water, and solvent, and reacted overnight. TEOS (Aldrich) was subsequently added in aliquots of 500 μL every 15 min to grow the siliceous shell after the synthesis of the dye-rich compact core was completed.

The synthesis of the expanded core was accomplished by co-condensing an aliquot (0.05 M) of TEOS with the dye precursor (containing 1.70×10^{-5} M of TRITC) and allowing it to complete overnight as described above. After the completion of the expanded core, the remainder of the TEOS was added in aliquots of 500 μL every 15 min for the growth of the silica shell.

Finally, the silica particles with homogeneous dye distribution were synthesized by co-condensing all reactants, that is, dye precursor and TEOS, at once. Briefly, ammonia source, solvent, and deionized water were mixed in a reaction vessel for about 30 min to allow the temperature to equilibrate. Next, a combination of the dye precursor and TEOS was added under vigorous stirring. After 30 min, the stirring speed was reduced, and the reaction allowed to complete overnight.

Fluorescence Correlation Spectroscopy. Fluorescence correlation spectroscopy (FCS) measurements were performed on a home-built instrument based on two-photon excitation.[25] The excitation source was a Ti:Sapphire femtosecond mode-locked laser driven by an Ar^+ ion laser pump (Spectra-Physics). The beam was positioned at the sample with a Bio-RAD MRC 600 scan box coupled to a Zeiss Axiovert 35 inverted microscope. Excitation light was focused with a Zeiss 63x C-Apochromat water immersion objective (N.A. = 1.2), and emission was collected through the same objective. The fluorescence was separated from the excitation with a 670 DCLP dichroic and passed through a HQ575/150 emission filter to a GaAsP photon-counting PMT (Hamamatsu). The resulting photocurrent was digitally autocorrelated with an ALV 6010 multiple tau autocorrelator.

The autocorrelation, $G(t)$, is defined as $\langle \delta F(t) \cdot \delta F(t+\tau) \rangle / \langle F(t) \rangle^2$, where $F(t)$ is the fluorescence at time t, $\delta F(t) = F(t) - \langle F(t) \rangle$,

(25) Larson, D. R. Optical Approaches to the Study of Nanoparticles and Biology: Quantum Dots, Silica Dots, and Retroviruses. Ph.D. Thesis, Cornell University, Ithaca, NY, 2003.

brackets denote ensemble averages, and τ is the delay. The fitting function is the standard function for one-component, three-dimensional diffusion assuming a prolate Gaussian focal volume:[26]

$$G(\tau) = \frac{1}{N}\left(1 + \frac{4D\tau}{w_{xy}^2}\right)^{-1}\left(1 + \frac{4D\tau}{w_z^2}\right)^{-1/2} \quad (1)$$

where w_{xy} and w_z are the lateral and axial dimensions of the two-photon focal volume, respectively;[25] N is the number of diffusing species in the focal volume; and D is the diffusion coefficient. All FCS measurements were carried out with an excitation wavelength of 900 nm. At this wavelength, the lateral dimension was determined to be 250 nm and the axial dimension to be 640 nm. The concentration calibration was determined from standard samples of rhodamine green to be 1.43 nM/particle (i.e., $N = 1$ corresponds to 1.43 nM).

Steady-State Spectroscopy. Absorbance measurements were done on a Cary 300 Bio UV/vis dual beam spectrophotometer. Fluorescence and excitation measurements were carried out on a PTI spectrofluorimeter. All steady-state spectroscopy was performed with one-photon excitation. All samples were measured in standard 10 × 10 mm four-sided clear plastic fluorometer cuvettes. The samples were first absorbance-matched to a free dye solution on the UV/vis spectrophotometer and then their fluorescence intensities immediately recorded on the spectrofluorimeter in the same sample holder.

Time-Resolved Spectroscopy. Time resolved fluorescence and anisotropy decays were measured using a two-photon excitation time-correlated single photon counting setup that has been described in detail elsewhere.[27] Fluorescence decays, $F(t)$, were measured using magic angle detection and fit using Becker & Hickl SPCImage 2.4 decay fitting software. The functional form used was

$$F(t) = F_{\text{baseline}} + F_0\sum_{i=1}^{n} a_i \exp(-(t - t_0)/\tau_i) \quad (2)$$

where n is the number of components; the decay time constants are τ_i; the amplitudes are a_i; F_{baseline} is the baseline fluorescence due to background; and F_0 is the peak fluorescence at time t_0, where t_0 is the temporal offset of the fluorescence decay from the start of data acquisition. The fitting routine effectively deconvolved the measured system response function. The amplitudes (a_i) satisfy the condition that $\sum_{i=1}^{n} a_i = 1$, and the average lifetime $\langle\tau\rangle$ is given by eq 3.

$$\langle\tau\rangle = \sum_{i=1}^{n} a_i\tau_i / \sum_{i=1}^{n} a_i \quad (3)$$

For time-resolved fluorescence anisotropy, parallel ($I_{||}(t)$) and perpendicular ($I_{\perp}(t)$) two-photon fluorescence decays were measured for equal acquisition times during which there was no significant fluctuation in the signal level. The measured anisotropy decay was then calculated from these polarization components and fit using the following functional form:[28,29]

$$r(t) = \left(\frac{I_{||}(t) - GI_{\perp}(t)}{I_{||}(t) + 2GI_{\perp}(t)}\right) = r_{\infty} + \sum_{i=1}^{m} r_{0i}\exp(-t/\theta_i) \quad (4)$$

The rotational correlation time (θ_i) for any given component was estimated along with both the initial (r_{0i}) and the residual (r_{∞}) anisotropy for hindered rotations. The average rotational correlation time for the mobile fraction is defined analogously to average lifetime, that is,

$$\langle\theta\rangle = \sum_{i=1}^{m} r_{0i}\theta_i / \sum_{i=1}^{m} r_{0i} \quad (5)$$

where the sum is over only the rotationally mobile components.

The G-factor describes the sensitivity of detection to polarization and was determined experimentally using tail-matching for free TRITC or coumarin decays. Under our experimental conditions, the optical depolarization due to the microscope objective (40×, 1.15 NA, with an underfilled back aperture) was negligible.[30,31] The system's temporal resolution of ~200 fs enabled observation of Förster resonance energy transfer but did not allow for observation of direct contact fluorescence quenching.

Results

The basic requirement for each nanoparticle architecture is monodispersity in aqueous solution, which has been estimated by FCS measurements (Figure 2 A−C). The FCS curve provides two critical, independent parameters: the diffusion coefficient and the concentration (1). The diffusion coefficient is directly related to the hydrodynamic radius, and the absolute concentration is important for quantifying photophysical parameters such as the number of dye molecules per particle. Furthermore, the goodness-of-fit to a one-component diffusion model is a good measure of monodispersity.[32] FCS curves for each nanoparticle architecture and its respective intermediate are shown in Figure 2 A−C with fits. For the compact core–shell architecture, the diffusion coefficient of the bare core (Figure 2 A, green curve, $D = 0.098$ μm^2/ms) is about half that of the free TRITC (Figure 2 A, red curve, $D = 0.21$ μm^2/ms). The complete core–shell particle is about 10 times bigger than the bare core (Figure 2A, blue curve, $D = 0.014$ μm^2/ms). A similar relationship among dye, core (Figure 2 B, green curve, $D = 0.075$ μm^2/ms), and core–shell (Figure 2 B, blue curve, $D = 0.013$ μm^2/ms) holds for the expanded core–shell particle. For the homogeneous architecture, there is no intermediate core structure, and the diffusion of the complete particle (Figure 2 C, blue curve, $D = 0.015$ μm^2/ms) is shown relative to free dye. The hydrodynamic radii calculated at 21 °C are tabulated in Table 1. Each nanoparticle curve is fit with a single diffusion coefficient, and the hydrodynamic sizes are equal within the error of the measurement (r =15 ± 1.2, 17 ± 1.4, and 15 ± 1.1 nm). For the core intermediates, the expanded core is slightly larger ($r = 2.9$ ± 0.3 nm) than the compact core ($r = 2.2 \pm 0.3$ nm). Note that the core represents only a small fraction of the total volume of the nanoparticle.

The amplitude $G(0)$ of the autocorrelation corrected for background fluorescence provides the number of particles in the effective focal volume, and the average count rate is a measure of the photons collected from the optically defined

(26) Thompson, N. L. *Fluorescence Correlation Spectroscopy*; Plenum Press: New York, 1991; p 337.
(27) Heikal, A. A.; Hess, S. T.; Webb, W. W. *Chem. Phys.* **2001**, *274*, 37.
(28) Lackowicz, J. R. *Principles of Fluorescence Spectroscopy*, 2nd ed.; Kluwer Academic: New York, 1999.
(29) O'Connor, D. V.; Phillips, D. *Time-Correlated Single Photon Counting*; Academic Press: London, 1984.
(30) Axelrod, D. *Biophys. J.* **1979**, *26*, 557–574.
(31) Axelrod, D. *Methods Cell. Biol.* **1989**, *30*, 333.
(32) Starchev, K.; Buffle, J.; Pérez, E. *J. Colloid Interface Sci.* **1999**, *213*, 479.

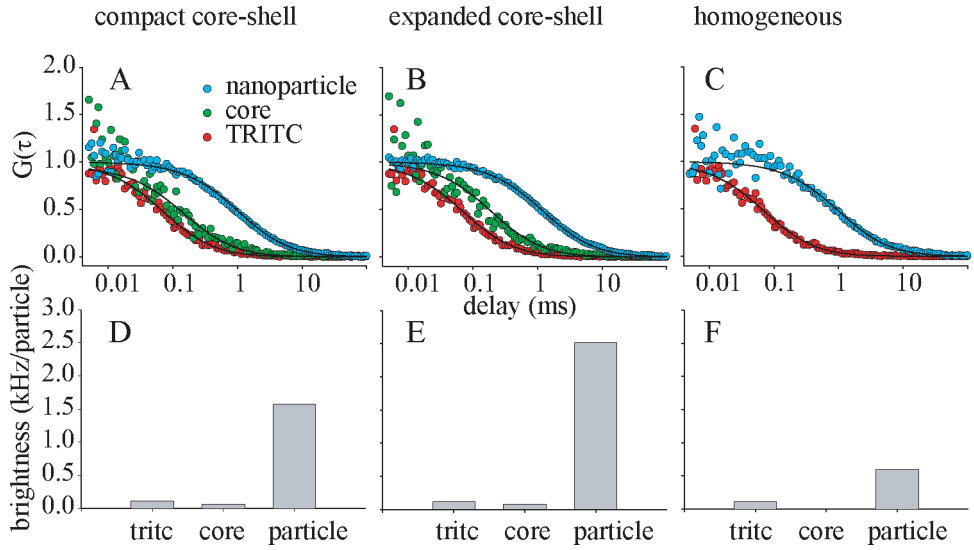

Figure 2. FCS of nanoparticles and synthetic intermediates. Panels A−C are the normalized autocorrelation curves. The red curve in panels A−C is free TRITC ($D = 0.21\ \mu m^2/ms$). (A) Compact core–shell particle. The green curve is the compact core ($D = 0.098\ \mu m^2/ms$); the blue curve is the compact core–shell nanoparticle ($D = 0.014\ \mu m^2/ms$). (B) Expanded core–shell particle. The green curve is the expanded core ($D = 0.075\ \mu m^2/ms$); the blue curve is the expanded core–shell nanoparticle ($D = 0.013\ \mu m^2/ms$). (C) Homogeneous particle. There is no core intermediate for the homogeneous particle; the blue curve is the complete homogeneous particle ($D = 0.015\ \mu m^2/ms$). Panels D−F are the brightness (counts/particle/second) for the synthesis stages of the compact core–shell architecture, expanded core–shell architecture, and the homogeneous architecture, respectively. Excitation: 1.2 mW at 900 nm.

Table 1. Hydrodynamic Radii of Nanoparticles and Nanoparticle Cores[a]

nanoparticle	core radius (nm)	core/shell radius (nm)
compact core/shell	2.2 (0.3)	15 (1.2)
expanded core/shell	2.9 (0.3)	17 (1.4)
homogeneous		15 (1.1)

[a] The hydrodynamic radii are determined from the Stokes–Einstein relationship and the diffusion coefficients measured by FCS. The standard deviation is included in parentheses.

focal volume.[33] One can thereby obtain the count rate per particle for each separable diffusing species, which provides a direct measure of their brightness.[27] The brightness of each architecture and the relevant synthesis intermediates, assuming negligible background correction, are shown in Figure 2 (D−F). For the syntheses which proceed with a core intermediate, the core is always dimmer than the free dye, despite the fact that many dye molecules are presumably present in the core, suggesting fluorescence quenching within the core.[24] In fact, the scatter in the correlation curve at short time for the core is due to low count rate/particle (Figure 2 A,B, green curves). However, it is noteworthy that the brightness of the complete nanoparticle can vary significantly for the same size particles made from the same absolute proportions of precursor materials.

To understand the photophysical properties of these nanoparticles, it is necessary to know both the number of TRITC molecules in the particle and the radiative properties of the TRITC within the particle. The effective number of TRITC molecules per particle can be estimated through a combination of FCS and absorbance measurements, in which the concentration of fluorescent particles is determined from FCS and the relative absorbance per particle is measured with respect to TRITC in solution (Figure 3 A−C). The absorbance is measured in units of optical density, and the fluorescence is scaled relative to TRITC, with the peak TRITC fluorescence scaled by the peak TRITC absorbance. Dilute solutions (~50 nM) were used so that the same sample could be used for both FCS and absorbance. The number of TRITC equivalents per particle, calculated using an extinction coefficient of 42 105 $M^{-1}\ cm^{-1}$ at 514.5 nm,[34] are compiled in Table 2. Likewise, the fluorescence quantum yield enhancement of the nanoparticles, relative to free TRITC, was calculated using the steady-state fluorescence and absorption spectra (Table 2). For the compact core–shell and the expanded core–shell, the number of TRITC per particle is indistinguishable at 8.6. However, the expanded core–shell shows a 3-fold enhanced fluorescence per TRITC over free dye, while the compact core–shell exhibits only a 2-fold enhancement (Figure 3 A,B, Table 2). The largest enhancement was observed for the homogeneous particle, which has on average only 2.3 dye molecules per particle (Figure 3 C, Table 2).

The estimation of TRITC equivalents is predicated on the assumption that the absorbance of TRITC does not change upon incorporation into the nanoparticle—an assumption which is not strictly correct. The nanoparticle absorption often deviates from absorption of free TRITC in water (for example, Figure 3A). More specifically, the absorption spectrum of the nanoparticle reveals an additional band that is not fluorescent according to the corresponding excitation spectra, which suggests a wavelength dependent quantum efficiency (Figure 3 D−F). For the compact core–shell architecture, the scaled absorbance (Figure 3D, red curve) is noticeably greater than the scaled excitation (Figure 3D, black curve) at wavelengths < 520 nm, suggesting that photons absorbed at short wavelengths have a relatively lower probability of leading to fluorescence than photons

(33) Mertz, J.; Xu, C.; Webb, W. W. *Opt. Lett.* **1995**, *20* (24), 2532.

(34) Soper, S. A.; Nutter, H. L.; Keller, R. A.; Davis, L. M.; Shera, E. B. *Photochem. Photobiol.* **1993**, *57* (6), 972.

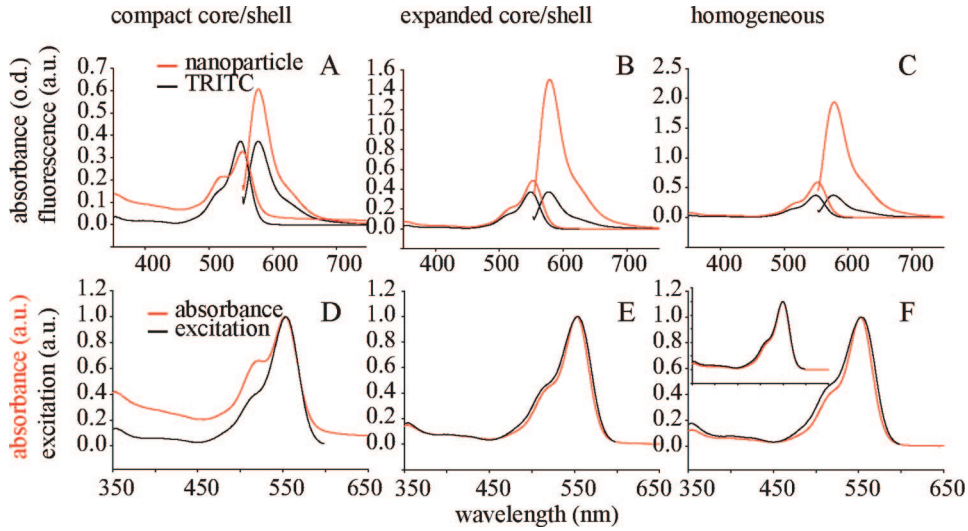

Figure 3. Steady state spectroscopy of nanoparticles. Panels A−C are the absorbance and fluorescence of the compact core–shell particle, expanded core–shell particle, and homogeneous particle, respectively. The absorbance is in real units of optical density. The fluorescence is scaled relative to TRITC. Nanoparticle spectra are in red; TRITC spectra are in black. Panels D−F are a comparison between absorbance and excitation for the compact core–shell particle, expanded core–shell particle, and homogeneous particle, respectively. Absorption spectra (red curves) and excitation spectra (black curves) are normalized to the maximum of the respective absorbance. The inset in panel F shows free TRITC absorbance and excitation.

Table 2. Relative Brightness of Silica Nanoparticles[a]

sample	TRITC equivalents	QE enhancement	brightness factor	counts/particle
TRITC	1.0 (0.2)	1.0 (0.1)	1.0	1.0 (0.1)
compact core/shell	8.6 (0.3)	2.0 (0.2)	18.0	14.0 (1.2)
expanded core/shell	8.7 (0.3)	3.1 (0.2)	27.0	22.0 (2.0)
homogeneous	2.3 (0.2)	3.3 (0.1)	7.5	6.0 (0.5)

[a] The brightness factor is the product of the number of TRITC equivalents of absorption per particle and the quantum efficiency (QE) enhancement. The counts/particle is determined from FCS. Values are normalized relative to free TRITC in water. The standard deviation is included in parentheses.

absorbed at longer wavelengths. This deviation is diminished in the other architectures, where the excitation curve (Figure 3 E,F, black curve) is the same or greater than the absorbance curve (Figure 3 E,F, red curve). The comparison between TRITC absorbance and excitation in solution is shown in Figure 3 F (inset). The number of TRITC equivalents (Table 2) is then determined from the peak value of absorbance (i.e., A_{552}) rather than an integrated value which would take into account possible nonfluorescent states appearing at shorter wavelengths.

The overall brightness enhancement of the particle, relative to free dye, is the product of the number of dye molecules inside the particle and the relative quantum efficiency enhancement of the encapsulated dye (Table 2, brightness factor). However, given the uncertainty in the determination of TRITC equivalents, it is necessary to have an additional, independent measure of brightness for comparison, such as the counts per particle measured from FCS (Table 2, counts/particle). The brightness factor is similar to the independent brightness determination from FCS (Table 2, comparing the last two columns), and the trend for brightness over the different architectures is the same by both methods. The brightness factor consistently overestimates the values measured by FCS, possibly as a result of the error in the determination of dye equivalents. Another possibility is that because the FCS measurement is done with polarized light, only a subset of the dye molecules within the particle is excited, leading to a counts/particle which is less than the brightness factor.

The measured brightness of the silica nanoparticles is therefore due both to incorporation of multiple dye molecules and to enhancement of the quantum efficiency of the incorporated dye molecules. This enhancement can be due, in general, to an increase in the radiative rate (k_r), a decrease in the nonradiative rate (k_{nr}), or both. The relative contributions of these factors are related to the average fluorescence lifetime (τ_f) and the quantum efficiency (φ) by

$$\langle \tau_f \rangle = \frac{1}{k_r + k_{nr}} \tag{6}$$

$$\varphi = \frac{k_r}{k_r + k_{nr}} \tag{7}$$

The fluorescence decay of the particles is shown in Figure 4 A. Each fluorescence decay is multiexponential, and the average lifetime values are compiled in Table 3. The average lifetime of TRITC ($\langle \tau_f \rangle = 2.1$ ns) is in good agreement with the literature value in water.[34] The lifetime increases from the compact core–shell (1.8 ns) to the expanded core–shell (2.9 ns) to the homogeneous particle (3.2 ns) (Figure 4 A). Interestingly, the compact core–shell has a lifetime which is less than that of free dye, although the dominant contribution to this lifetime is a fast component (Figure 4 A, green curve). From this lifetime data alone, one might conclude that the dye is quenched inside the compact core–shell particle, in contrast to steady state measurements. However, the combination of both measurements allows for a unique determination of the radiative and nonradiative rate constants (Table 3). The enhancement of the radiative rate is independent of particle architecture and is 2.2-fold greater than free TRITC. However, the nonradiative rate is sensitive to internal architecture and varies from a relative high value for the compact core–shell particles to a value almost 3-fold less for the homogeneous particles.

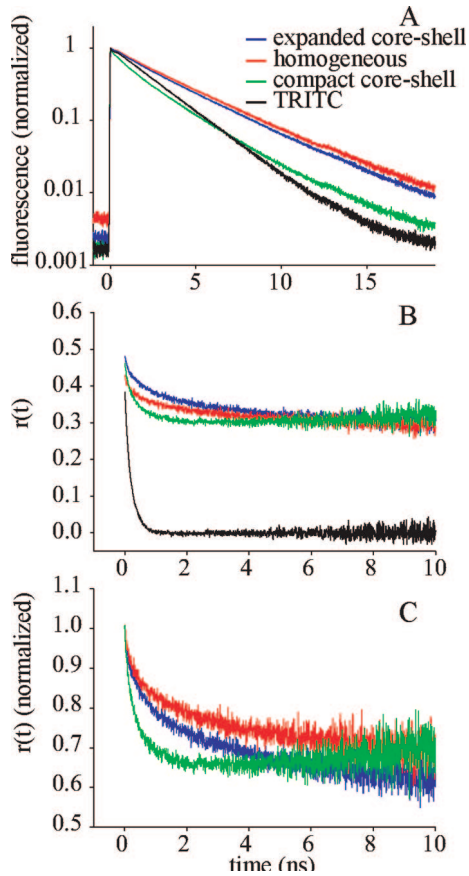

Figure 4. Time-resolved fluorescence of nanoparticles. (A) Normalized fluorescence decay of homogeneous particle (red), expanded core–shell (blue), compact core–shell (green), and TRITC (black). (B) Fluorescence anisotropy of expanded core–shell (blue), homogeneous (red), compact core–shell (green), and TRITC (black). (C) Normalized fluorescence anisotropy of nanoparticle curves shown in B. Average fit values for the fluorescence lifetime ($\langle t_f \rangle$) and rotational lifetime ($\langle q \rangle$) are compiled in Table 3.

To elucidate the underlying relationship between the nonradiative pathway and the nanoparticle architecture, we have measured the time-resolved fluorescence anisotropy of these nanoparticles. The rotational anisotropy of the particles again shows complicated, multiexponential behavior (Figure 4 B,C), and we restrict quantitative analysis to the average rotational time constant (Table 3, $\langle \theta \rangle$). As expected, the rotation of the dye inside the particle is hindered by the silica matrix, leading to longer rotation times than free dye (Figure 4B). The anisotropy curves do not decay to zero on the time scale of the measurement, in contrast to the TRITC control, because the particle rotational diffusion times are far longer than the fluorescence decay times. However, there is still a remarkable degree of rotational mobility, even inside the tightly packed core of the particle. The time scales of rotation are too fast to be the overall rotation of the entire 30 nm particle and too slow to be depolarization due to energy transfer, which occurs on the picosecond time scale.[14] Furthermore, the amplitudes of the nanoparticle anisotropy curves (r_0) are the same or greater than free TRITC and are near the theoretical amplitude for two-photon anisotropy ($r_0 = 0.57$),[35] suggesting that there is not the fast depolarization usually associated with energy transfer.

It is therefore likely that the decay in anisotropy is due to hindered rotation of the dye molecules within the silica matrix. The scaled anisotropy for each architecture is shown in Figure 4C. The compact core–shell particle has the fastest, least hindered rotation (green curve), followed by the expanded core–shell particle (blue curve), and finally the homogeneous particle (red curve). This rotation time has a monotonic, inverse dependence on the nonradiative rate constant (Table 3), suggesting that the confined mobility in the silica particle is responsible for suppression of nonradiative decay.

Discussion

We have demonstrated that photophysical properties of dye molecules can be manipulated upon encapsulation within 30 nm silica particles. This control is accomplished through changes in silica architecture on the nanometer size scale and results in enhanced fluorescence quantum efficiency of the constituent dye compared to free dye. The quantum efficiency increase is due both to an increase in the radiative rate and a decrease in the nonradiative rate, with the latter effect being the most variable between architectures. The changes in nonradiative rate correspond to differences in rotational mobility of the dye within the particle.

The observed changes in radiative and nonradiative rates are greater than those observed for free TRITC in various solvents or conjugations to molecules. Soper et al. measured photophysical constants for TRITC under a variety of conditions and found at most a 30% increase in the radiative rate compared to free, unbound TRITC in water.[34] The maximum reduction in nonradiative rate was also $\sim$ 30%. For silica nanoparticles, we have observed a greater than 2-fold increase in the radiative rate and a 3-fold reduction in the nonradiative rate.

The 2-fold increase in radiative rate is retained across the different architectures, suggesting a direct interaction between the dye and the silica matrix that is independent of architecture. One possible explanation for the increased radiative rate is the increase in index of refraction within the silica. Toptygin et al. have derived an expression for the radiative rate of a fluorophore embedded in a small dielectric ellipsoid of refractive index n_1 which is surrounded by a dielectric material of refractive index n_0.[36] This relationship predicts that if the surrounding refractive index n_0 is increased relative to the local refractive index n_1, the radiative rate can increase as well. For free dye in water, the fluorophore is considered to be in an empty ellipsoidal cavity ($n_1 = 1.00$) surrounded by a homogeneous dielectric fluid ($n_0 = 1.33$; eq 34 from ref 36). If this analogy is extended to dye in the nanoparticle, the fluorophore would be in an empty ellipsoidal cavity surrounded by the silica matrix, which in turn contains and is surrounded by water. The fluorophore does exhibit rotational motion within the nanoparticle, suggesting that the local cavity model is relevant. Furthermore, the theoretically derived enhancement of the radiative rate is strongly dependent on the geometry of the cavity and

(35) Geddes, C. D. *J. Fluoresc.* **2002**, *12* (314), 343.

(36) Toptygin, D.; Savtchenko, R. S.; Meadow, N. D.; Roseman, S.; Brand, L. *J. Phys. Chem. B* **2002**, *106*, 3724.

Table 3. Time-Resolved Fluorescence Parameters for Silica Nanoparticles[a]

sample	$\langle\tau_f\rangle$ (ns)	φ	k_r (ns^{-1})	k_r normalized	k_{nr} (ns^{-1})	k_{nr} normalized	$\langle\theta\rangle$ (ns)
TRITC	2.1	0.15[b]	0.072	1.0	0.41	1.0	0.21
compact core–shell	1.8	0.30	0.17	2.3	0.39	0.95	0.40
expanded core–shell	2.9	0.47	0.16	2.2	0.18	0.45	3.1
homogeneous	3.2	0.50	0.16	2.2	0.16	0.39	5.9

[a] Absolute fluorescence lifetimes $\langle\tau_f\rangle$ and rotational lifetimes $\langle\theta\rangle$ are the weighted average of a multicomponent fit. Radiative rate (k_r) and nonradiative rate (k_{nr}) are determined from eqs 6 and 7 (φ is quantum efficiency). Normalized values are with respect to TRITC in water. The fluorescence quantum yields are measured relative to free TRITC. [b] Absolute quantum efficiency of TRITC from Soper et al.[34]

the orientation of the transition dipole within the cavity. Assuming a prolate ellipsoidal cavity ($L_m = 0.75$ in Toptygin's original notation) and using the measured refractive index for dye-doped silica ($n = 1.46$)[13] results in an enhancement factor of 2.2, which is the factor we observe experimentally (Table 3).

In contrast to the radiative rate, the nonradiative rate changes by almost a factor of 3 between nanoparticle architectures. This decrease in nonradiative rate is likely due to the stabilization of the chromophore within the silica environment, as evidenced by corresponding changes in the rotational mobility. As the molecular structure becomes rigid, conformational changes (i.e., isomerization) and vibrational relaxation during the excited-state lifetime are hindered, resulting in less efficient nonradiative rates and consequently enhanced fluorescence emission. Other factors might also be responsible for changes in nonradiative rate between architectures. For example, the compact core–shell shows a significant nonfluorescent absorption peak at 520 nm (Figure 3D) which is not present in the expanded core–shell. This shoulder is attributable to a dimerization interaction which is known to occur for rhodamine and which is apparently more significant at higher effective concentrations of dye.[37,38] In addition, the protection of the chromophore from the solvent environment might also lead to a reduction in nonradiative rate.

One process which does not appear to lead to quenching in the nanoparticles is intraparticle energy transfer. In the presence of energy transfer, one expects a fast depolarization (~1 ps), which shows up as a decreased r_0 in anisotropy measurements.[14] The fact that the amplitudes of the nanoparticle anisotropy curves are close to the theoretical r_0 and the r_0 of TRITC suggests that there is little (if any) energy transfer, even for the compact core–shell particle (Figure 4 B). This finding is surprising in light of the size of the nanoparticles, in which the characteristic distance based on isotropic arrangement of molecules is on the order of 2–3 nm for the core–shell particles. In comparison for TRITC using literature values for the extinction coefficient and quantum efficiency in water[34] we calculated for the Förster radius, R_0; that is, the distance at which energy transfer is 50% efficient, a value of $R_0 = 37$ Å, which is consistent with literature values.[39] One possibility is that the fluorophores are arranged along the outside of the core, at the interface between the core and the shell, thus reducing the packing density of the dye. This speculation is also supported by the large increase in brightness going from the core to the complete core–shell particle (Figure 2 D−F). It is also possible that there is an orientational configuration of the dye molecules along this core–shell interface which is not conducive to energy transfer.

The lack of conspicuous energy transfer in the nanoparticle suggests that dye molecules within the particle are absorbing and emitting independently. Furthermore, the approximate agreement between the brightness factor (product of the number of TRITC equivalents and the quantum efficiency enhancement) and the counts/molecule determined by FCS (Table 2) also argues that dye molecules can absorb and emit independently. The presence of multiple emitters is critical to the brightness of the nanoparticle and is one significant difference between dye-doped nanoparticles and quantum dots. Quantum dot fluorescence proceeds more or less through a single readily stimulated exciton, while the silica nanoparticle fluorescence appears to be the result of multiple excitons. This difference accounts for the similarities in brightness observed for quantum dots and silica nanoparticles.[24] In addition, the presence of multiple emitters in a single, nanometer-sized particle might also be useful for photonics applications. We note also that fluorescence "blinking" is not observed in FCS measurements on silica nanoparticles, making them potentially effective as single particle labels.

Conclusion

Designing silica nanoparticles to achieve modified photophysical properties of constituent dye enables novel exploitation of the vast diversity of organic dye molecules. For example, dyes with large absorption cross-section and low quantum efficiency might become viable fluorophores when encapsulated in nanoparticles.[40,41] More than one dye can be incorporated in the particles leading, for example, to ratiometric sensor particles.[21] Furthermore, silica nanoparticles are water-soluble, can be made multifunctional through the modular synthesis approach, and are easily surface functionalized—important characteristics to generate highly integrated and highly functional nanomaterials for biological applications and assembly of novel structured materials.[42]

(37) Ravdin, P.; Axelrod, D. *Anal. Biochem.* **1977**, *80*, 585.
(38) Meadows, D. L.; Shafer, J. S.; Schultz, J. S. *J. Immunol. Methods* **1991**, *143*, 263.
(39) Massey, M.; Algar, W. R.; Krull, U. J. *Anal. Chim. Acta* **2006**, *568*, 181.
(40) Albota, M.; Beljonne, D.; Bredas, J.; Ehrlich, J. E.; Fu, J.; Heikal, A. A.; Hess, S. E.; Kogej, T.; Levin, M. D.; Marder, S. R.; McCord-Maughon, D.; Perry, J. W.; Rockel, H.; Rumi, M.; Subramaniam, G.; Webb, W. W.; Wu, X.; Xu, C. *Science* **1998**, *281*, 1653.
(41) Herz, E.; Burns, A.; Lee, S.; Sengupta, P.; Bonner, D.; Ow, H.; Liddell, C.; Baird, B.; Wiesner, U. *Proc. SPIE-Int. Soc. Opt. Eng.* **2006**, *6096*, 609605.
(42) Choi, J.; Burns, A. A.; Williams, R. M.; Zhou, Z.; Flesken-Nikitin, A.; Zipfel, W. R.; Wiesner, U.; Nikitin, A. Y. *J. Biomed. Opt.* **2007**, *12*, 064007.

Acknowledgment. This publication was developed under the auspices of the Cornell University Center for Biotechnology, New York State Center for Advanced Technology, supported by New York State and industrial partners. The work was further supported by the Cornell Center for Materials Research (CCMR) with funding from the Materials Research Science and Engineering Center program of the National Science Foundation (cooperative agreement DMR 0520404). The work was also supported by NSF Grant DBI-0080792 and NIBIB-NIH Grant 9 P41 EB001976 (D.R.L., H.D.V., A.A.H., W.W.W.). D.R.L. was supported by the Nanobiotechnology Center (NBTC), an STC program of the NSF under Agreement No. ECS-9876771. H.D.V. was supported by the NIH-NIGMS Molecular Biophysics Training Grant GM08267.

CM7026866